NANO LETTERS

pubs.acs.org/NanoLett Letter

Charge Oscillations in Bilayer Graphene Quantum Confinement Devices

Hailong Fu,* Ke Huang, Kenji Watanabe, Takashi Taniguchi, and Jun Zhu*

Cite This: https://doi.org/10.1021/acs.nanolett.3c02253 Read Online

ACCESS | Metrics & More | Article Recommendations | Supporting Information

ABSTRACT: Quantum confinement structures are building blocks of quantum devices in fundamental physics exploration and technological applications. In this work, we fabricate dual-gated bilayer graphene Fabry−Pérot quantum Hall interferometers employing two different gating strategies and conduct finite element simulations to understand the electrostatics of the confinement structures and to guide device design and fabrication. We observe two types of resistance oscillations arising from the charging of quantum dots formed inside the interferometers. We obtain the size, location, and charging energy of the dots by measuring the dependence of the oscillations on the magnetic field, gate voltages, and dc bias. We analyze and discuss the origin of the quantum dots and their impact on quantum Hall edge state backscattering and interference. Insights gained in these studies shed light on the construction of van der Waals quantum confinement devices.

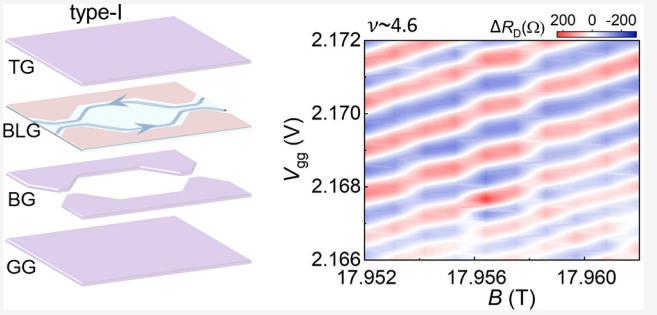

KEYWORDS: *Quantum Hall effect, Fabry−Pérot interferometer, Quantum dot, Quantum oscillation, Charging energy*

Elemental quantum confinement structures such as a quantum point contact (QPC) and quantum dot play foundational roles in illuminating the mesoscopic physics of 2D semiconductors and the realization of spin and charge qubits.[1−3] In the quantum Hall effect, QPCs and two-QPC interferometers are essential tools to determine charge and statistics of many-body excitations and probe non-Abelian states and topological orders.[4−12] These challenging experiments place stringent requirements on the quality of the two-dimensional electron gas (2DEG), device fabrication, and measurement conditions. Each material faces its own challenges. GaAs possesses the highest-quality 2DEG and straightforward gate-defined confinement but suffers from complications such as edge reconstruction due to a soft confinement potential.[13−15]

High-quality monolayer and bilayer graphene-based quantum confinement devices use thin hexagonal-boron nitride (h-BN) sheets as gate dielectrics.[16−33] The resulting confinement potential is typically sharper than that in GaAs and the nearby gates offer effective screening. Aharonov−Bohm (AB) oscillations at integer quantum Hall states have been observed recently in monolayer graphene[30−32] and bilayer graphene (BLG),[33] respectively. An electric-field-induced band gap in BLG makes it possible to adopt existing strategies in 2D semiconductors to construct mesoscopic devices. Research on BLG spin and valley qubits has progressed rapidly.[24−26] In addition, BLG hosts even-denominator fractional quantum Hall states with large gaps of a few Kelvin[34−37] and is therefore a promising material to realize non-Abelian statistics, which is foundational to topological quantum computing.[4]

In this work, we report on the design and construction of gate-defined BLG Fabry−Pérot quantum Hall interferometers employing two novel gating structures that have been unreported in the past. Finite element simulations are used to understand the electrostatics of both structures and to guide the fabrication of devices. Prominent resistance oscillations periodic in the magnetic field and gate voltages are observed, and our analyses show that they arise from the charging of quantum dots formed inside the interferometers. We obtain properties of the dots in terms of their size, charging energy, and location and discuss their impact on edge state backscattering and interference. Because quantum Hall interferometry is extremely sensitive to disorder, knowledge gained here will be useful to the construction of other quantum confinement structures, including qubits.

Figure 1a and b show respectively the schematic 3D stacking view of two interferometer designs we explored. They are different from those used in refs 30, 31, and 33. Both include three layers of gates with h-BN as gate dielectrics and

Received: June 15, 2023
Revised: October 4, 2023

https://doi.org/10.1021/acs.nanolett.3c02253
Nano Lett. XXXX, XXX, XXX−XXX

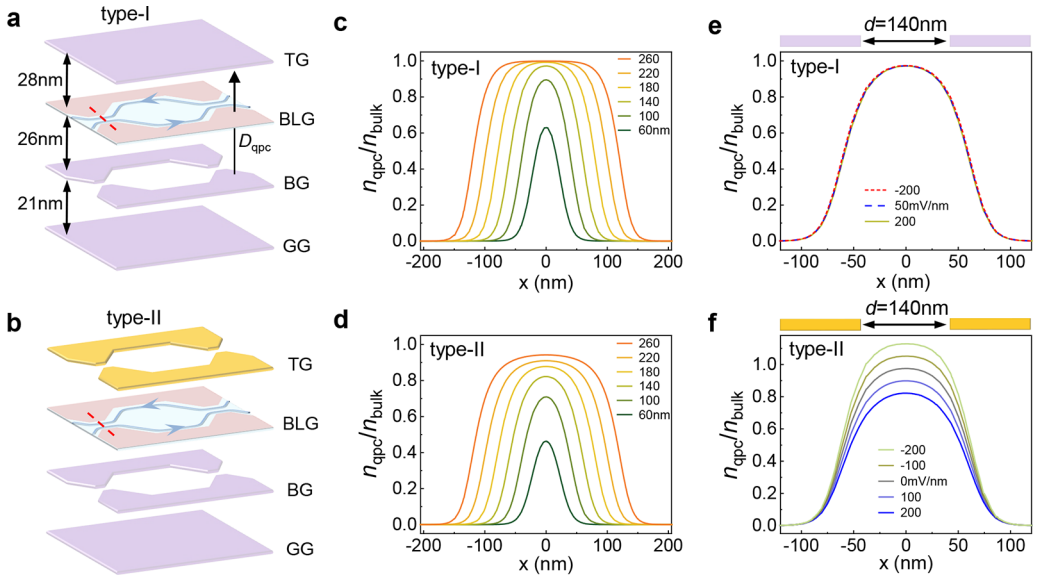

Figure 1. Structure schematics and finite element simulations of BLG quantum Hall interferometers. a and b show 3D stacking of type-I and type-II devices, respectively, using h-BN as gate dielectric layers (not shown). The etched graphite BGs define the interferometer loop in both structures. Type-I devices use a whole graphite piece as the TG while type-II devices use split gold TG aligned with the split BG. Dual-gated areas are shaded pink and are kept at mid gap by applying a large displacement field D as illustrated. $D > 0$ points up. c and d show the simulated carrier density profile n_{qpc}/n_{bulk} across a QPC opening along the red dashed line in a and b in type-I and -II structures, respectively. Simulations use the h-BN layer thicknesses of device D1 marked in a. $D_{qpc} = 200$ mV/nm. Constant bulk density $n_{bulk} = 1.7 \times 10^{12}$ cm^{-2} corresponds to $\nu = 4$ at $B = 18$ T. Different traces correspond to different opening sizes d as labeled in the plots. e and f show the simulated carrier density profile n_{qpc}/n_{bulk} as a function of D_{qpc} in type-I and -II devices, respectively. Here $d = 140$ nm is fixed in both calculations.

additionally a silicon back-gate to dope the contact areas separately, which is not shown. Type-I structure (Figure 1a, devices 607 or D1 and 622 or D2) includes a graphite top grate (TG), a split graphite bottom gate (BG) etched to form an interferometer loop with two QPCs, and a graphite global gate (GG). Device D2 also contains a side bottom gate (see Figure S1 in SI). Through the use of a large, perpendicular electric displacement field D, we open a band gap in the areas dual-gated by the TG and BG and place the Fermi level at mid gap.[16,17] Similar to past practices in GaAs, this gate-controlled band insulator creates a confinement potential. The carrier density inside and outside the interferometer n_{bulk} is tuned by a combination of the TG and GG. A strong advantage of the type-I design is the screening provided by the TG and GG, which improves the BLG quality[33,37] and reduces the charging energy of the interferometer, which was critically important in the observation of fractional charge and statistics in GaAs.[8,9] In the type-II structure shown in Figure 1b (device 605 or D3), the graphite TG is replaced by lithographically patterned split metallic gates that align vertically with the BG to create the confinement.[16,17,28] This structure leaves the interferometer area open to other stimuli, e.g., RF radiation, which will be important for qubit operations.[1,3] The GG is used to control n_{bulk} of the interferometer although we will see soon that voltages on the confinement gates, i.e., the TG and BG, have a considerable effect on the carrier density inside the QPC, n_{qpc}.

We first examine the gating characteristics of the interferometers using finite element simulations (COMSOL multiphysics package) following methods described in our previous works.[16,22] Though the calculations are based on classical electromagnetics, our previous results show that they capture the effects of the gates very well. Figure 1c,d plot examples of simulated carrier density profiles $n_{qpc}(x)$ across the opening of a QPC in type-I,II structure, respectively. The simulations use the thickness of the h-BN dielectric layers in device D1 shown in Figure 1a. Common to both structures, as the size of the QPC opening d narrows, the GG is increasingly screened by the BG, leading to reduced carrier density inside the QPC (electron carrier in this scenario, $n_{qpc} < n_{bulk}$). This effect is more pronounced in type-II structures. The dependence of n_{qpc} on D_{qpc} used to generate the confinement, however, is qualitatively different in the two structures. In type-I structures, $n_{qpc}(x)$ is independent of D_{qpc}, since to keep a constant bulk carrier density, the GG must covary with the TG and BG, resulting in a steady $n_{qpc}(x)$ profile as shown in Figure 1e. Thus, in type-I interferometers the edge state backscattering rate is only controlled by the size of the QPC opening d and not D_{qpc}. In type-II structures, because of the absence of another top gate above the QPC opening, the fringe effect of the split TG dominates that of the split BG. Thus, a positive/negative D_{qpc} means a negative/positive gate voltage on the TG and consequently decreased/increased n_{qpc} as shown in Figure 1f ($D_{qpc} > 0$ is defined as pointing from BG to TG). Indeed our measurements, which are shown in Figure S2 of the SI, support the D_{qpc} dependence revealed in Figure 1e and f. Insights obtained in the simulations guided the design and construction of our interferometers, and we expect them to be useful to the fabrication of other quantum confined devices in BLG as well.[24−26]

We fabricated both type-I (devices D1 and D2) and type-II (device D3) devices, the parameters of which are summarized in Table 1. Figure 2a and b show the optical micrographs of devices D1 and D3, respectively. Figure 2c shows an atomic force microscopy (AFM) image of the etched BG in device D1. Device fabrications utilize dry van der Waals transfer, reactive ion etch, annealing, and precision alignment techniques.[16] A detailed description is given in the Methods. We obtain the characteristics of the gates following established practices.[16,17]

https://doi.org/10.1021/acs.nanolett.3c02253
Nano Lett. XXXX, XXX, XXX−XXX

Table 1. Device Parameters

device (type)	TG/BG/GG gating efficiency α ($\times 10^{11}$ V^{-1} cm^{-2})	QPC opening d (nm)	lithographic interferometer area A (μm^2)
607 (I) or Dl	6.0/6.4/3.6	140	1
622 (I) or D2	7.9/10.4/4.2	220	2.7
605 (II) or D3	9.8/7.6/4.2	110	1

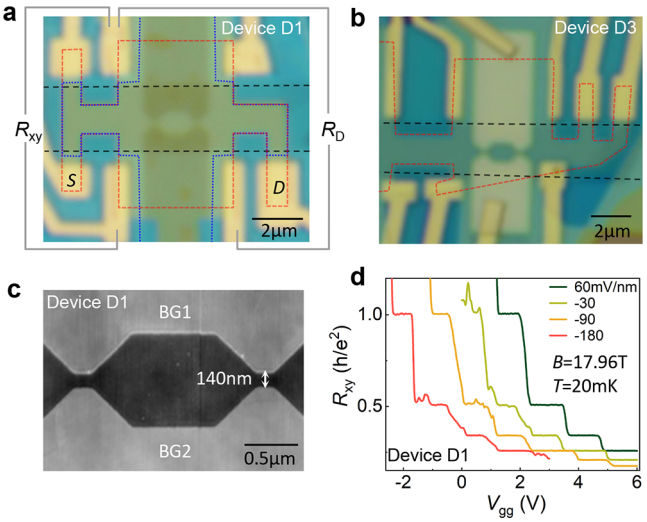

Figure 2. Device images and characterization. a and b show optical micrographs of devices D1 (type-I) and D3 (type-II), respectively. The red dashed lines outline the profile of the BLG sheet. The black dashed lines outline the profile of the global graphite gate. The blue dotted lines in panel a outline the profile of the top graphite gate in device D1. In device D3, the gold split TG and graphite split BG align in position. An AFM image of the graphite BG in device D1 is shown in c. The QPC opening d = 140/110 nm in device D1/D3, respectively. We measure the Hall resistance R_{xy} and the diagonal resistance R_D across the interferometer simultaneously as illustrated in a. d shows exemplary traces of R_{xy} vs V_{gg} in device D1. Traces correspond to different D_{qpc}'s as labeled in the plot. R_{xy} exhibits well developed integer quantum Hall plateaus over a wide range of parameters. Traces from devices D3 and D2 are shown in Figure S2 of the SI.

All of our gates worked well and behaved as expected. A typical D_{qpc} used to define the QPCs ranges −400 to +400 mV/nm. We measure Hall resistance R_{xy} on the left or right side of the interferometer to probe the properties of the bulk BLG and measure the diagonal resistance R_D across the interferometer to probe the transmission of quantum Hall edge states as illustrated in Figure 2a. Figure 2d shows traces of R_{xy} vs the gate voltage on the GG, V_{gg}, at a series of D_{qpc} values in device D1. A larger D_{qpc} means more hole doping from the TG and consequently the same filling factor ν shifts to a larger V_{gg}. This is indeed what our data showed. Integer quantum Hall states ν = 1, 2, 3, 4, 5, and 6 are well developed. Characteristic traces of devices D2 and D3 are given in Figure S2 of the SI and show well-developed integer quantum Hall states too.

We begin with the discussion of device D1, which has a QPC opening of d = 140 nm as shown in Figure 2c. Figure 3a plots together the R_{xy} of the bulk and R_D through the interferometer as a function of V_{gg}. At this opening, our simulations in Figure 1c suggest an n_{qpc} only slightly smaller than n_{bulk} and thus weakly backscattered edge states. However, the measured $R_D(V_{gg})$ is considerably larger than the corresponding $R_{xy}(V_{gg})$, indicating significant edge state backscattering. In addition, $R_D(V_{gg})$ exhibits prominent resistance oscillations over a wide range of filling factors, magnetic fields and at temperatures $T \lesssim 0.3$ K. The resistance oscillations are periodic in both V_{gg} and B over large stretches. Figure 3b and c show magnified views of the oscillations taken near the locations marked by the color-coded arrows in Figure 3a while large range scans are given in Figure S3a and b of the SI. Both the periods in B and V_{gg} are ν-dependent, suggesting that a simple AB interference model cannot explain our data. In the literature, R_D oscillations originate from two major mechanisms.[5,6] The first is the AB effect, where the phase difference of the interfering edge states $\phi = BA$ is tuned by the magnetic field with a period $\Delta B = \phi_0/A$ inversely proportional to A, the area of the interferometer loop. $\phi_0 = h/e$ is the magnetic flux quantum. ΔB does not explicitly depend on ν, but A may change with ν and the edge potential. A gate can also induce resistance oscillations by affecting the interferometer area. For electrons, a more positive ΔV_{gg} enlarges A, thus a negative ΔB is needed to maintain a constant ϕ. In a second mechanism, R_D oscillations can also arise from single-electron Coulomb charging effects.[6,38] In an intuitive picture introduced in ref 38, the interior of the entire interferometer, or a portion of it, consists of two parts: a charge island (quantum dot) of size A_D containing $(\nu-\nu_D)B$ electrons and ν_D underlying filled Landau levels (LLs). While the total charge is controlled by V_{gg}, a changing magnetic field mimics the effect of a gate to the island by changing the charge occupation of the underlying ν_D filled LLs. A magnetic field increase of $\Delta B = {}^{\phi_0}/_{A_D\nu_D}$ (eq 1) increases the electron number of the filled ν_D LLs by 1, thus reducing the electron number in the island by 1; thus maintaining a constant charge number in the island requires a *positive* $\Delta V_{gg} = {}^{1}/_{\alpha_{gg}A_D}$ (eq 2), where α_{gg} is the gating efficiency of the GG, or another gate that couples to the dot. A crucial test to differentiate these two mechanisms is to examine the slope of $\Delta B/\Delta V_{gg}$ in a constant phase/charge contour plot.[8,9,38] Figure 3d plots a 2D false-color map of $R_D(B,V_{gg})$ taken at $\nu \sim 4.6$. The positive slopes in Figure 3d indicate that these R_D oscillations are dominated by Coulombic charging effects.

We quantitatively analyze the oscillations following the charging scenario. ΔB obtained at different fields and filling factors are used to determine the quantum dot area A_D using eq 1, and the results are plotted in Figure 3e for different V_{gg}'s. Using the measured ΔV_{gg} and the values of A_D in Figure 3e, we calculate the product $\Delta V_{gg}A_D\alpha_{gg}$ and plot the results in Figure 3f. The values of $\Delta V_{gg}A_D\alpha_{gg}$ fall between 0.92 and 1.13, in good agreement with unity expected from eq 2. The dot area A_D increases from 0.20 to 0.31 μm^2 as the carrier density n_{bulk} increases from 1.38×10^{12} to 2.01×10^{12} cm^{-2}. A_D is only a fraction of the area of the interferometer loop A = 1.0 μm^2, suggesting that the quantum dot is formed by unintentional potential variations inside the interferometer loop. As such, the increase in A_D with increasing electron density is quite reasonable. We estimate the total charging energy of a dot to be $E_c = 1/2\ e^2/C_{tot} \approx e\Delta V_{gg}/5.34$. Here, $C_{tot} = C_{tg} + C_{gg} + C_{bg1} + C_{bg2} \approx C_{tg} + C_{gg} = 2.67C_{gg}$ since $C_{tg} = 1.67C_{gg}$ and $C_{bg1} = C_{bg2} \cong 0$ (see Figure S4 of the SI). Our measurements of ΔV_{gg} in Figure 3c and Figure S3d of the SI yield E_c in the range of 0.16 to 0.27 meV. This agrees well with a Coulomb diamond

https://doi.org/10.1021/acs.nanolett.3c02253
Nano Lett. XXXX, XXX, XXX−XXX

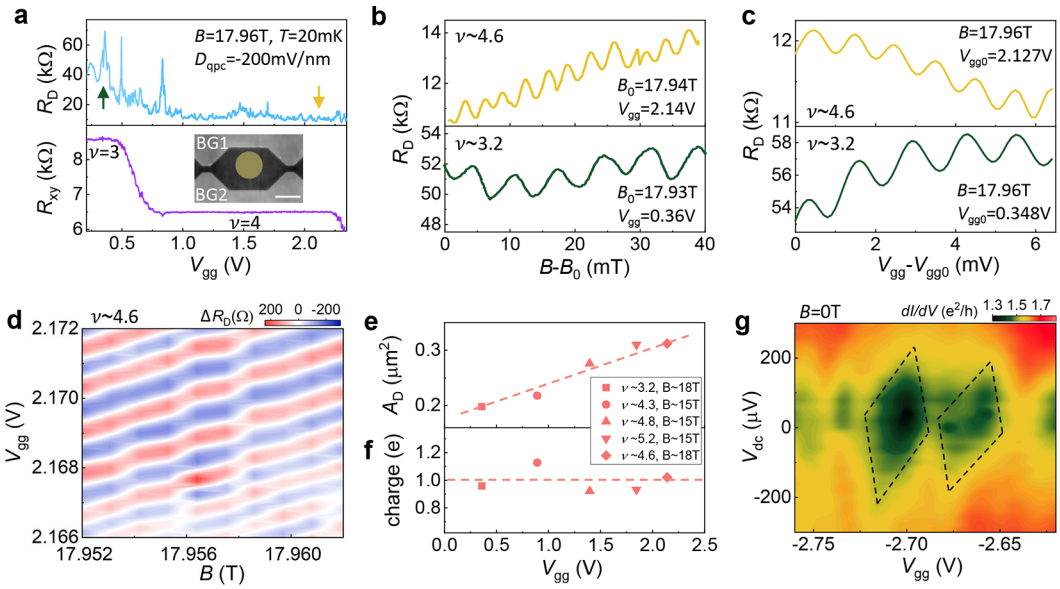

Figure 3. Coulomb charging induced resistance oscillations in device D1. (a) R_{xy} (bottom panel) and R_D (top panel) vs V_{gg} near filling factors $\nu = 3$ and 4. b and c show R_D-B and R_D-V_{gg} oscillations around the locations marked by the color-coded arrows in a. The R_D-B oscillation period is approximately 6.97/3.32 mT at $\nu \sim 3.2/4.6$. The R_D-V_{gg} oscillation period is approximately 1.36/0.92 mV at $\nu \sim 3.2/4.6$. d shows a false-color map of $R_D(V_{gg},B)$ taken at $\nu \sim 4.6$, the positive slope of which supports the Coulomb-blockade origin of the resistance oscillations. A smooth background is subtracted. e and f show quantum dot size A_D calculated using eq 1 and the product $\Delta V_{gg}A_D\alpha_{gg}$ calculated at different magnetic fields and filling factors as labeled in the plot. The underlying ν_D is 3 for $\nu \sim 3.2$, 4 for $\nu \sim 4.3$ and 4.6, and 5 for $\nu \sim 4.8$ and 5.2. The calculated product fluctuates around the expected value of 1. This plot includes ΔB and ΔV_{gg} extracted from additional measurements given in Figure S3 of the SI. The dashed lines are a guide to the eye. g shows a false-color map of $dI/dV(V_{dc},V_{gg})$. $B = 0$ T, $T = 20$ mK, and $D_{qpc} = -200$ mV/nm. Black dashed lines are a guide to the eye, from which we estimate a charging energy of 0.18−0.22 meV. This corresponds to a quantum dot of approximately 0.27−0.33 μm^2, illustrated in the inset of panel a. The dot is closer to BG1, as given by the different oscillation periods of R_D-V_{bg1} and R_D-V_{bg2} (Figure S4 of the SI). The scale bar in the inset is 0.5 μm.

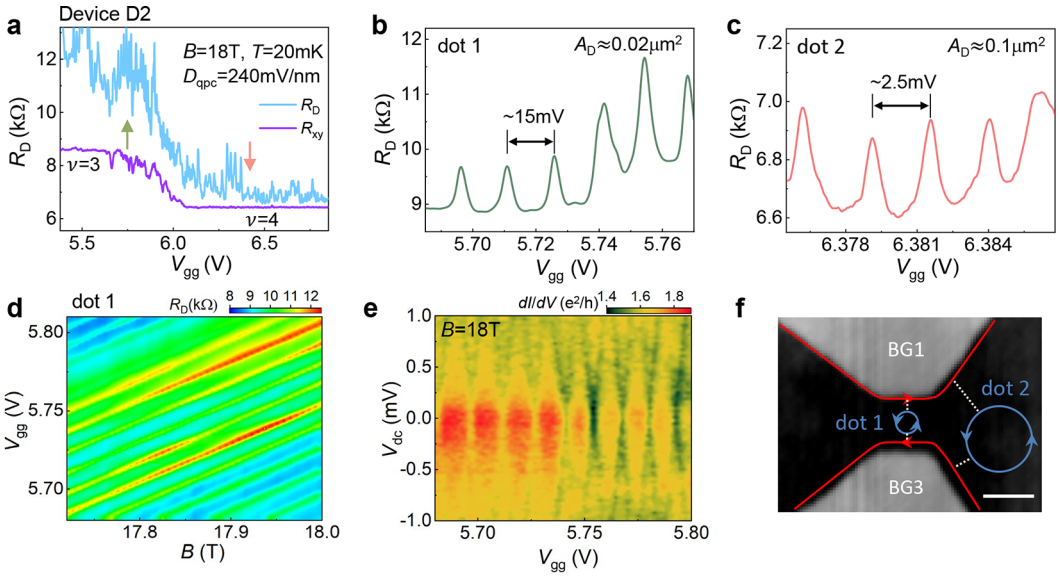

Figure 4. Quantum dot mediated edge state backscattering in device D2. a shows the Hall resistance R_{xy} (purple trace) and the diagonal resistance R_D (blue trace). $B = 18$ T, $T = 20$ mK, and $D_{qpc} = 240$ mV/nm unless otherwise mentioned. b and c show expanded R_D-V_{gg} around the locations marked by the color-coded arrows in a. ΔV_{gg} is approximately 15 mV in b and 2.5 mV in c, corresponding to dot 1 with an area of $A_D = 0.02$ μm^2 and dot 2 with an area of $A_D = 0.1$ μm^2, respectively. d shows a false-color map of $R_D(V_{gg},B)$ from dot 1. A similar map from dot 2 is shown in Figure S6 of the SI. Both show that the observed resistance oscillations are charge dominated. The extracted magnetic field periods (~60 mT from dot 1 and ~10 mT from dot 2) from the maps are used to calculate the dot areas using eq 1. e shows a false-color map of $dI/dV(V_{dc},V_{gg})$ from dot 1. $dI/dV(V_{dc},V_{gg})$ exhibits "inverted" diamonds, where the conductance decreases with increasing V_{dc}, in contrast to the conductance through a conventional quantum dot. This observation, together with the R_D peaks shown in b and c, points to quantum dot resonance mediated edge state backscattering near a QPC. This situation is illustrated in f, overlaying the AFM image of the left QPC formed by BG1 and BG3 in device D2. The red lines represent the innermost edge states, the blue lines the quantum dots, and the white dashed lines resonant backscattering pathways. We infer the location of the dots from the charging efficiencies of different gates shown in Figure S6. The scale bar in f is 0.2 μm.

https://doi.org/10.1021/acs.nanolett.3c02253
Nano Lett. XXXX, XXX, XXX−XXX

plot $dI/dV(V_{dc},V_{gg})$ obtained at $B = 0$ T and shown in Figure 3g, which gives an estimated $E_c \approx 0.18-0.22$ meV.

Measurements performed on devices D3 and D2 have also uncovered R_D oscillations consistent with Coulomb charging dominated oscillations, where similar analyses have led to quantum dot size ranging from 0.02 to 0.1 μm^2, all of which are considerably smaller than their respective lithographically defined interferometer areas. Figure S5 of the SI plots an example of a very small dot in device D3, where we find $A_D = 0.05$ μm^2. Further, despite the large QPC openings chosen to position our interferometers in the weak backscattering regime of the edge states, all our devices exhibit a R_D considerably larger than R_{xy} in operation (see, for example, Figure 3a and Figure 4a). These observations suggest that unintentional scatterers were introduced to our devices, especially near the QPC opening area.

We present a second type of resistance oscillation exhibited by some of our devices. Figure 4a plots $R_D(V_{gg})$ and $R_{xy}(V_{gg})$ near $\nu = 3$ and 4 in device D2, where $d = 220$ nm. R_D is approximately 12 kΩ at $\nu = 3$. Data around the locations marked by the green ($\nu = 3$) and red ($\nu = 4$) arrows are expanded in Figure 4b and c, and yield $\Delta V_{gg} \approx 15$ mV (dot 1) and 2.5 mV (dot 2), respectively. Oscillations of dot 1 appear around $\nu = 3$ and 4, while dot 2 only manifests around $\nu = 4$. These oscillations are also dominated by Coulomb charging effects, as indicated by the positively sloped stripes of the $R_D(B,V_{gg})$ map shown in Figure 4d. Using eq 1, we determine the size of the corresponding quantum dots to be approximately $A_D = 0.02$ μm^2 (dot 1) and 0.1 μm^2 (dot 2), respectively, in stark contrast to the lithographic interferometer size of $A = 2.7$ μm^2 in device D2. Different from the oscillations shown in Figure 3, here the resonant charging events of the dots correspond to *resistance* peaks in R_D, i.e., enhanced edge state backscattering, instead of enhanced transmission as expected from a conventional quantum dot. Figure 4e shows the "diamond plot" $dI/dV(V_{dc},V_{gg})$ of dot 1 at $B = 18$ T, where a conductance suppression at the tip of the diamond further confirms the "inverted" nature of the resistance oscillations. This situation is reminiscent of resonantly enhanced edge state backscattering reported in ref 39. For this mechanism to be effective, dots 1 and 2 should be located inside or near the opening of the QPCs. In this scenario, the backscattering between edge states traveling along the upper and lower edges of the QPC is generally enhanced because of the presence of the dot, leading to a large R_D observed in our devices and a resistance peak when a charge state of the dot is resonant at the Fermi level. By studying the dependence of R_D on different bottom gates (Figure S6 in the SI), we deduce that both dots 1 and 2 are in the vicinity of the left QPC formed by BG1 and BG3, and dot 2 is closer to BG3, as schematically illustrated in Figure 4f.

The ubiquitous Coulomb charging induced resistance oscillations made it difficult to discern the effect of AB interference in our interferometers. Their presence suggests that unintentional potential fluctuations were introduced in the device fabrication step, especially near the QPCs. The fabrication of both types of interferometers involves the removal of stamp residue in between van der Waals transfer steps, and this could be a potential source of contamination. However, we consider it unlikely as we can routinely achieve ultrahigh-quality devices that undergo similar procedures.[37] Another possible source of potential fluctuation comes from transferring an h-BN/BLG/h-BN stack to the patterned bottom gates that are raised a few nanometers from the surface. An uneven adherence of the stack could lead to inhomogeneous gating, which may have led to the formation of the observed quantum dots. The understanding and control of these processes will be crucial to the development of the BLG quantum confinement devices. Quantum Hall interferometry is particularly sensitive to imperfections and serves as a good touchstone experiment.

We fabricated two types of bilayer graphene Fabry–Pérot interferometer devices guided by finite element simulations and observed Coulomb charging dominated oscillations that correspond to quantum dots of different sizes inside the interferometers. The unanticipated quantum dots, while disruptive to the AB interference effect, serve to illuminate potential experimental challenges faced by van der Waals stacked graphene heterostructures, which are distinct from conventional semiconductor 2D systems. Insights gained in these studies are useful for experiments working on other gate-defined graphene mesoscopic devices.

METHODS

Device Fabrication. We use the conventional van der Waals dry transfer technique and PPC stamps to make stacks. The devices are fabricated using the following procedure: (1) Transfer a h-BN/global graphite gate (GG) stack to a doped Si/SiO_2 substrate. (2) Anneal the stack in Ar/O_2 atmosphere at 450 °C for 3 h to remove polymer residue on the stack surface. (3) Exfoliate the bottom graphite sheet onto a PPC stamp and transfer it to the h-BN/GG stack. (4) Pattern and etch the bottom graphite sheet to form the interferometer structure with two QPCs. (5) Anneal the stack again and characterize it using AFM. In this step, we obtain the QPC opening d and the lithographic interferometer area A. (6) Transfer a h-BN/BLG/h-BN stack to the BG/h-BN/GG stack. (7) For type-I devices, anneal the stack again and then transfer the top graphite sheet to the stack using the same technique as transferring the bottom graphite sheet. (8) Define the Hall bar structure using e-beam lithography and reactive ion etching (CHF_3/O_2 plasma). (9) Pattern and deposit Cr/Au (5/45 nm) contacts. (10) For type-II devices, pattern and deposit Ti/Au (5/20 nm) top gates that vertically align with the etched bottom gates. In this step, the precision alignment techniques developed in ref.[16] are used to limit the misalignment, which can be as small as 10 nm.

Transport Measurement. The devices were measured in a He3 system and in a dilution refrigerator at the NHMFL (SCM 1) employing standard low-frequency ($f = 17.777$ Hz) lock-in techniques (SR860). Resistance measurements use a small ac excitation current of 1 nA, generated by using the internal ac voltage source of SR860 with a load resistor of 100 MΩ. Bias-dependent conductance measurements use a combination of a small ac excitation voltage of 10 μV and varying dc excitation voltages generated by using the internal ac+dc voltage source of SR860 with a 1000:1 divider. Gate voltages are applied by using either a Yokogawa GS200 or Keithley 2450.

ASSOCIATED CONTENT

Supporting Information

The Supporting Information is available free of charge at https://pubs.acs.org/doi/10.1021/acs.nanolett.3c02253.

https://doi.org/10.1021/acs.nanolett.3c02253
Nano Lett. XXXX, XXX, XXX−XXX

Device images and characteristics and additional Coulomb dominated resistance oscillations in three devices (PDF)

AUTHOR INFORMATION

Corresponding Authors

Hailong Fu − *Department of Physics, The Pennsylvania State University, University Park, Pennsylvania 16802, United States; School of Physics, Zhejiang University, Hangzhou 310058, China;* orcid.org/0000-0001-5928-2979; Email: hailongfu@zju.edu.cn

Jun Zhu − *Department of Physics, The Pennsylvania State University, University Park, Pennsylvania 16802, United States; Center for Two-Dimensional and Layered Materials, The Pennsylvania State University, University Park, Pennsylvania 16802, United States;* orcid.org/0000-0001-8100-967X; Email: jzhu@phys.psu.edu

Authors

Ke Huang − *Department of Physics, The Pennsylvania State University, University Park, Pennsylvania 16802, United States;* orcid.org/0000-0001-8521-6465

Kenji Watanabe − *Research Center for Electronic and Optical Materials, National Institute for Materials Science, Tsukuba 305-0044, Japan;* orcid.org/0000-0003-3701-8119

Takashi Taniguchi − *Research Center for Materials Nanoarchitectonics, National Institute for Materials Science, Tsukuba 305-0044, Japan;* orcid.org/0000-0002-1467-3105

Complete contact information is available at: https://pubs.acs.org/10.1021/acs.nanolett.3c02253

Author Contributions

H.F. and J.Z. designed the experiment. H.F. fabricated the devices and made the measurements. K.H. assisted in device fabrication and measurement. H.F. and J.Z. analyzed the data. K.W. and T.T. synthesized the h-BN crystals. H.F. and J.Z. wrote the manuscript with input from all authors.

Notes

The authors declare no competing financial interest.

ACKNOWLEDGMENTS

This work is supported by the Kaufman New Initiative research grant no. KA2018-98553 of the Pittsburgh Foundation and by the National Science Foundation through the grant NSF-DMR-1904986. H.F. acknowledges the support of the Penn State Eberly Research Fellowship and the ZJU 100 Talents Program of Zhejiang University. K.W. and T.T. acknowledge support from the JSPS KAKENHI (Grant Numbers 20H00354, 21H05233, and 23H02052) and World Premier International Research Center Initiative (WPI), MEXT, Japan. Work performed at the National High Magnetic Field Laboratory is supported by the National Science Foundation Cooperative Agreement No. DMR-2128556 and the State of Florida. We thank Dr. Elizabeth Green for assisting in measurements at the National High Magnetic Field Laboratory.

REFERENCES

(1) Hanson, R.; Kouwenhoven, L. P.; Petta, J. R.; Tarucha, S.; Vandersypen, L. M. K. Spins in few-electron quantum dots. *Rev. Mod. Phys.* **2007**, *79* (4), 1217−1265.

(2) van Houten, H.; Beenakker, C. W. J.; Wees, B. J. v. Chapter 2: Quantum Point Contacts. In *Semiconductors and Semimetals*; Reed, M., Ed.; Elsevier, 1992; Vol. *35*, pp 9−112.

(3) Vandersypen, L. M. K.; Eriksson, M. A. Quantum computing with semiconductor spins. *Phys. Today* **2019**, *72* (8), 38−45.

(4) Nayak, C.; Simon, S. H.; Stern, A.; Freedman, M.; Das Sarma, S. Non-Abelian anyons and topological quantum computation. *Rev. Mod. Phys.* **2008**, *80* (3), 1083−1159.

(5) de C. Chamon, C.; Freed, D. E.; Kivelson, S. A.; Sondhi, S. L.; Wen, X. G. Two point-contact interferometer for quantum Hall systems. *Phys. Rev. B* **1997**, *55* (4), 2331−2343.

(6) Halperin, B. I.; Stern, A.; Neder, I.; Rosenow, B. Theory of the Fabry-Perot quantum Hall interferometer. *Phys. Rev. B* **2011**, *83* (15), 155440.

(7) Bartolomei, H.; Kumar, M.; Bisognin, R.; Marguerite, A.; Berroir, J. M.; Bocquillon, E.; Plaçais, B.; Cavanna, A.; Dong, Q.; Gennser, U.; Jin, Y.; Fève, G. Fractional statistics in anyon collisions. *Science* **2020**, *368* (6487), 173−177.

(8) Nakamura, J.; Liang, S.; Gardner, G. C.; Manfra, M. J. Direct observation of anyonic braiding statistics. *Nat. Phys.* **2020**, *16* (9), 931−936.

(9) Nakamura, J.; Fallahi, S.; Sahasrabudhe, H.; Rahman, R.; Liang, S.; Gardner, G. C.; Manfra, M. J. Aharonov−Bohm interference of fractional quantum Hall edge modes. *Nat. Phys.* **2019**, *15* (6), 563−569.

(10) Banerjee, M.; Heiblum, M.; Umansky, V.; Feldman, D. E.; Oreg, Y.; Stern, A. Observation of half-integer thermal Hall conductance. *Nature* **2018**, *559* (7713), 205−210.

(11) Dutta, B.; Yang, W.; Melcer, R.; Kundu, H. K.; Heiblum, M.; Umansky, V.; Oreg, Y.; Stern, A.; Mross, D. Distinguishing between non-abelian topological orders in a Quantum Hall system. *Science* **2022**, *375*, No. 193.

(12) Willett, R. L.; Shtengel, K.; Nayak, C.; Pfeiffer, L. N.; Chung, Y. J.; Peabody, M. L.; Baldwin, K. W.; West, K. W. Interference Measurements of Non-Abelian e/4 & Abelian e/2 Quasiparticle Braiding. *Phys. Rev. X.* **2023**, *13* (1), 011028.

(13) Wan, X.; Yang, K.; Rezayi, E. H. Reconstruction of Fractional Quantum Hall Edges. *Phys. Rev. Lett.* **2002**, *88* (5), 056802.

(14) Venkatachalam, V.; Hart, S.; Pfeiffer, L.; West, K.; Yacoby, A. Local thermometry of neutral modes on the quantum Hall edge. *Nat. Phys.* **2012**, *8* (9), 676−681.

(15) Sabo, R.; Gurman, I.; Rosenblatt, A.; Lafont, F.; Banitt, D.; Park, J.; Heiblum, M.; Gefen, Y.; Umansky, V.; Mahalu, D. Edge reconstruction in fractional quantum Hall states. *Nat. Phys.* **2017**, *13* (5), 491−496.

(16) Li, J.; Wang, K.; McFaul, K. J.; Zern, Z.; Ren, Y.; Watanabe, K.; Taniguchi, T.; Qiao, Z.; Zhu, J. Gate-controlled topological conducting channels in bilayer graphene. *Nat. Nanotechnol.* **2016**, *11* (12), 1060−1065.

(17) Li, J.; Zhang, R.-X.; Yin, Z.; Zhang, J.; Watanabe, K.; Taniguchi, T.; Liu, C.; Zhu, J. A valley valve and electron beam splitter. *Science* **2018**, *362* (6419), 1149−1152.

(18) Zimmermann, K.; Jordan, A.; Gay, F.; Watanabe, K.; Taniguchi, T.; Han, Z.; Bouchiat, V.; Sellier, H.; Sacépé, B. Tunable transmission of quantum Hall edge channels with full degeneracy lifting in split-gated graphene devices. *Nat. Commun.* **2017**, *8* (1), 14983.

(19) Wei, D. S.; van der Sar, T.; Sanchez-Yamagishi, J. D.; Watanabe, K.; Taniguchi, T.; Jarillo-Herrero, P.; Halperin, B. I.; Yacoby, A. Mach-Zehnder interferometry using spin- and valley-polarized quantum Hall edge states in graphene. *Sci. Adv.* **2017**, *3* (8), No. e1700600.

(20) Polshyn, H.; Zhou, H.; Spanton, E. M.; Taniguchi, T.; Watanabe, K.; Young, A. F. Quantitative Transport Measurements of Fractional Quantum Hall Energy Gaps in Edgeless Graphene Devices. *Phys. Rev. Lett.* **2018**, *121* (22), 226801.

(21) Zeng, Y.; Li, J. I. A.; Dietrich, S. A.; Ghosh, O. M.; Watanabe, K.; Taniguchi, T.; Hone, J.; Dean, C. R. High-Quality Magnetotransport in Graphene Using the Edge-Free Corbino Geometry. *Phys. Rev. Lett.* **2019**, *122* (13), 137701.

(22) Li, J.; Wen, H.; Watanabe, K.; Taniguchi, T.; Zhu, J. Gate-Controlled Transmission of Quantum Hall Edge States in Bilayer Graphene. *Phys. Rev. Lett.* **2018**, *120* (5), 057701.
(23) Kumar, C.; Srivastav, S. K.; Das, A. Equilibration of quantum Hall edges in symmetry-broken bilayer graphene. *Phys. Rev. B* **2018**, *98* (15), 155421.
(24) Eich, M.; Herman, F.; Pisoni, R.; Overweg, H.; Kurzmann, A.; Lee, Y.; Rickhaus, P.; Watanabe, K.; Taniguchi, T.; Sigrist, M.; Ihn, T.; Ensslin, K. Spin and Valley States in Gate-Defined Bilayer Graphene Quantum Dots. *Phys. Rev. X.* **2018**, *8* (3), 031023.
(25) Banszerus, L.; Möller, S.; Icking, E.; Watanabe, K.; Taniguchi, T.; Volk, C.; Stampfer, C. Single-Electron Double Quantum Dots in Bilayer Graphene. *Nano Lett.* **2020**, *20* (3), 2005−2011.
(26) Gächter, L. M.; Garreis, R.; Gerber, J. D.; Ruckriegel, M. J.; Tong, C.; Kratochwil, B.; de Vries, F. K.; Kurzmann, A.; Watanabe, K.; Taniguchi, T.; Ihn, T.; Ensslin, K.; Huang, W. W. Single-Shot Spin Readout in Graphene Quantum Dots. *PRX Quantum* **2022**, *3* (2), 020343.
(27) Ahmad, N. F.; Komatsu, K.; Iwasaki, T.; Watanabe, K.; Taniguchi, T.; Mizuta, H.; Wakayama, Y.; Hashim, A. M.; Morita, Y.; Moriyama, S.; Nakaharai, S. Fabry−Pérot resonances and a crossover to the quantum Hall regime in ballistic graphene quantum point contacts. *Sci. Rep.* **2019**, *9* (1), 3031.
(28) Fu, H.; Huang, K.; Watanabe, K.; Taniguchi, T.; Zhu, J. Gapless Spin Wave Transport through a Quantum Canted Antiferromagnet. *Phys. Rev. X.* **2021**, *11* (2), 021012.
(29) Jo, M.; Brasseur, P.; Assouline, A.; Fleury, G.; Sim, H. S.; Watanabe, K.; Taniguchi, T.; Dumnernpanich, W.; Roche, P.; Glattli, D. C.; Kumada, N.; Parmentier, F. D.; Roulleau, P. Quantum Hall Valley Splitters and a Tunable Mach-Zehnder Interferometer in Graphene. *Phys. Rev. Lett.* **2021**, *126* (14), 146803.
(30) Déprez, C.; Veyrat, L.; Vignaud, H.; Nayak, G.; Watanabe, K.; Taniguchi, T.; Gay, F.; Sellier, H.; Sacépé, B. A tunable Fabry−Pérot quantum Hall interferometer in graphene. *Nat. Nanotechnol.* **2021**, *16* (5), 555−562.
(31) Ronen, Y.; Werkmeister, T.; Haie Najafabadi, D.; Pierce, A. T.; Anderson, L. E.; Shin, Y. J.; Lee, S. Y.; Lee, Y. H.; Johnson, B.; Watanabe, K.; Taniguchi, T.; Yacoby, A.; Kim, P. Aharonov−Bohm effect in graphene-based Fabry−Pérot quantum Hall interferometers. *Nat. Nanotechnol.* **2021**, *16* (5), 563−569.
(32) Zhao, L.; Arnault, E. G.; Larson, T. F. Q.; Iftikhar, Z.; Seredinski, A.; Fleming, T.; Watanabe, K.; Taniguchi, T.; Amet, F.; Finkelstein, G. Graphene-Based Quantum Hall Interferometer with Self-Aligned Side Gates. *Nano Lett.* **2022**, *22* (23), 9645−9651.
(33) Fu, H.; Huang, K.; Watanabe, K.; Taniguchi, T.; Kayyalha, M.; Zhu, J. Aharonov−Bohm Oscillations in Bilayer Graphene Quantum Hall Edge State Fabry−Pérot Interferometers. *Nano Lett.* **2023**, *23* (2), 718−725.
(34) Ki, D.-K.; Fal'ko, V. I.; Abanin, D. A.; Morpurgo, A. F. Observation of Even Denominator Fractional Quantum Hall Effect in Suspended Bilayer Graphene. *Nano Lett.* **2014**, *14* (4), 2135−2139.
(35) Li, J. I. A.; Tan, C.; Chen, S.; Zeng, Y.; Taniguchi, T.; Watanabe, K.; Hone, J.; Dean, C. R. Even-denominator fractional quantum Hall states in bilayer graphene. *Science* **2017**, *358* (6363), 648−652.
(36) Zibrov, A. A.; Kometter, C.; Zhou, H.; Spanton, E. M.; Taniguchi, T.; Watanabe, K.; Zaletel, M. P.; Young, A. F. Tunable interacting composite fermion phases in a half-filled bilayer-graphene Landau level. *Nature* **2017**, *549* (7672), 360−364.
(37) Huang, K.; Fu, H.; Hickey, D. R.; Alem, N.; Lin, X.; Watanabe, K.; Taniguchi, T.; Zhu, J. Valley Isospin Controlled Fractional Quantum Hall States in Bilayer Graphene. *Phys. Rev. X.* **2022**, *12* (3), 031019.
(38) Zhang, Y.; McClure, D. T.; Levenson-Falk, E. M.; Marcus, C. M.; Pfeiffer, L. N.; West, K. W. Distinct signatures for Coulomb blockade and Aharonov-Bohm interference in electronic Fabry-Perot interferometers. *Phys. Rev. B* **2009**, *79* (24), 241304.
(39) Goldman, V. J.; Su, B. Resonant Tunneling in the Quantum Hall Regime: Measurement of Fractional Charge. *Science* **1995**, *267* (5200), 1010−1012.

https://doi.org/10.1021/acs.nanolett.3c02253
Nano Lett. XXXX, XXX, XXX−XXX